JOURNAL OF AIRCRAFT
Vol. 32, No. 2, March–April 1995

Computation of Passively Controlled Transonic Wing

I. Kim* and B. Sung†
Korea Aerospace Research Institute, Taejon 305-333, Republic of Korea

A computational investigation has been conducted to examine the effect of passive control on the transonic wing flowfield. The effect of passive control was included through the use of a porous surface over a vent chamber on the upper surface of a wing. The passive control was numerically simulated by the use of a linear form of the Darcy pressure law. The solutions of the three-dimensional Euler equations were generated using the finite volume multistage Runge-Kutta time-stepping scheme. The computational results indicated that the fundamental behavior of passive control is two dimensional in nature, but spanwise variations of the passive control effect exist.

Introduction

THE passive control concept has been studied as a economical method to improve the performance of a transonic airfoil. This concept consists of replacing a part of the airfoil upper surface by a porous plate with a vent chamber beneath it (Fig. 1). Since the pressure behind the shock is greater than the pressure in front of the shock, by locating the vent chamber in the shock foot region, a natural forcing mechanism exists by which to passively drive blowing and suction of air through the porous surface. In a transonic airfoil with well-designed porous surface, the air blowing process produces a thickening of the boundary layer ahead of the shock and this thickening in turn generates a series of compression waves that suppresses the shock. In this manner the entropy change across the shock is reduced, to achieve a smaller drag, and the drag rise Mach number was increased.

The effectiveness of passive control has been proved by previous experiments.[1-4] They applied the control concept on a circular-arc or airfoil model on a Mach number range of 0.7–0.9, and showed that passive control can be effective in shock suppression or drag reduction. In particular, Krogmann et al.[4] observed that passive control is also effective in postponing the onset of buffet on a transonic supercritical airfoil. In addition, numerical solutions are obtained to improve the understanding of the control concept by implementing full potential theory,[5] full potential code coupled with boundary-layer code,[6,7] and thin layer Navier-Stokes code.[8] On the other hand, ideas realizing the control effects in different ways are also suggested. Ma et al.[9] proposed that the passive control mechanism can be activated by implementing an elastic membrane wall instead of a porous wall. Hartwich[10] demonstrated the feasibility of using the porous airfoils to achieve the multipoint design.

The objective of the present work is to investigate the role of passive control on a three-dimensional configuration, since previous studies were mostly confined in two-dimensional analysis. In this work we assess the effect of passive control on the flow structure by comparing the flow over the solid and porous ONERA M6 wing.

Received June 14, 1993; presented as Paper 93-3474 at the AIAA Applied Aerodynamics Conference, Monterey, CA, Aug. 9–11, 1993; revision received May 10, 1994; accepted for publication May 19, 1994.

*Senior Researcher, Aerodynamics Department, 52 Oun-Dong, Yusung-Gu. Member AIAA.

†Head, Aerodynamics Department, 52 Oun-Dong, Yusung-Gu. Member AIAA.

Governing Equations

The motion of an inviscid compressible fluid is governed by the Euler equations. The equations subject to the three-dimensional general coordinate transformation may be written in dimensionless, conservation-law form as

$$\frac{\partial \tilde{U}}{\partial t} + \frac{\partial \tilde{E}}{\partial \xi} + \frac{\partial \tilde{F}}{\partial \eta} + \frac{\partial \tilde{G}}{\partial \zeta} = 0 \tag{1}$$

where $\tilde{U}$, $\tilde{E}$, $\tilde{F}$, and $\tilde{G}$ are the following vectors:

$$\tilde{U} = J^{-1}U = J^{-1}\begin{bmatrix} \rho \\ \rho u \\ \rho v \\ \rho w \\ \rho E \end{bmatrix} \tag{2}$$

$$\tilde{E} = J^{-1}\begin{bmatrix} \rho\tilde{u} \\ \rho\tilde{u}u + \xi_x p \\ \rho\tilde{u}v + \xi_y p \\ \rho\tilde{u}w + \xi_z p \\ \rho\tilde{u}H \end{bmatrix} \tag{3}$$

$$\tilde{F} = J^{-1}\begin{bmatrix} \rho\tilde{v} \\ \rho\tilde{v}u + \eta_x p \\ \rho\tilde{v}v + \eta_y p \\ \rho\tilde{v}w + \eta_z p \\ \rho\tilde{v}H \end{bmatrix} \tag{4}$$

$$\tilde{G} = J^{-1}\begin{bmatrix} \rho\tilde{w} \\ \rho\tilde{w}u + \zeta_x p \\ \rho\tilde{w}v + \zeta_y p \\ \rho\tilde{w}w + \zeta_z p \\ \rho\tilde{w}H \end{bmatrix} \tag{5}$$

Here, ρ and p denote the density and pressure, respectively. The total energy per unit volume E is defined for a perfect gas by

$$E = [p/(\gamma - 1)] + \tfrac{1}{2}\rho(u^2 + v^2 + v^2) \tag{6}$$

where γ is the ratio of specific heats.

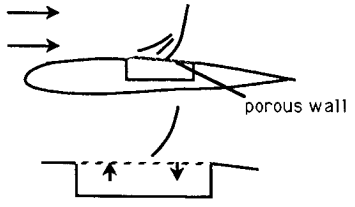

Fig. 1 Passive control for a transonic airfoil.

The transformation Jacobian J is defined as

$$J = \xi_x\eta_y\zeta_z + \xi_y\eta_x\zeta_x + \xi_x\eta_x\zeta_y = -\xi_x\eta_x\zeta_y - \xi_z\eta_y\zeta_x - \xi_y\eta_x\zeta_z \tag{7}$$

The so-called contravariant velocity components used in Eqs. (2–5) are obtained from Cartesian velocity components u, v, and w as

$$\tilde{u} = \xi_x u + \xi_y v + \xi_z w$$
$$\tilde{v} = \eta_x u + \eta_y v + \eta_z w \tag{8}$$
$$\tilde{w} = \zeta_x u + \zeta_y v + \zeta_z w$$

Numerical Procedure

The governing equations, Eq. (1), while written in generalized coordinates, are used in a finite volume formulation. The computational domain is divided into hexahedral cells. The location of the nodes of which the flowfield variables are computed are the centers of the cells formed by the grid points. Integration of Eq. (1) over a cell volume Ω and bounding surface $\partial\Omega$ gives

$$\int\int\int_\Omega \frac{\partial \bar{U}}{\partial t}\,d\Omega + \int\int\int_\Omega \left(\frac{\partial \tilde{E}}{\partial \xi} + \frac{\partial \tilde{F}}{\partial \eta} + \frac{\partial \tilde{G}}{\partial \zeta}\right) d\Omega = 0 \tag{9}$$

Using Green's theorem to transform the second volume integral to a surface integral for each cell, one can write the governing equations in the semidiscrete form as

$$\frac{\partial \bar{U}}{\partial t} + (\tilde{E}_{i+1/2,j,k} - \tilde{E}_{i-1/2,j,k}) + (\tilde{F}_{i,j+1/2,k} - \tilde{F}_{i,j-1/2,k}) + (\tilde{G}_{i,j,k+1/2} - \tilde{G}_{i,j,k+1/2}) = 0 \tag{10}$$

where

$$\tilde{E}_{i\pm 1/2,j,k} = \tfrac{1}{2}(\tilde{E}_{i,j,k} + \tilde{E}_{i\pm 1,j,k})$$
$$\tilde{F}_{i,j\pm 1/2,k} = \tfrac{1}{2}(\tilde{F}_{i,j,k} + \tilde{F}_{i,j\pm 1,k})$$
$$\tilde{G}_{i,j,k\pm 1/2} = \tfrac{1}{2}(\tilde{G}_{i,j,k} + \tilde{G}_{i,j,k\pm 1})$$

Eq. (10) may be written in the form

$$\frac{d}{dt}(J^{-1}_{i,j,k}U_{i,j,k}) + Q_{i,j,k} = 0 \tag{11}$$

where $Q_{i,j,k}$ is the net flux out of the cell.

In order to suppress any odd-even point decoupling in the numerical solution and to damp oscillations in the vicinity of the shock waves and stagnation points, artificial dissipation terms are added to the finite volume scheme. With dissipation terms, Eq. (11) may be replaced by

$$\frac{d}{dt}(J^{-1}U) + Q(U) - D(U) = 0 \tag{12}$$

where $D(U)$ represents the added artificial dissipation term. The artificial dissipation term used in this article is the model devised by Jameson et al.[11,12] Detailed description of artificial dissipation model can be found in the literature.

The steady-state solution was obtained by integrating Eq. (12) using a four-stage Runge-Kutta scheme.[11,12] Since the mesh used in this study is independent of time, Eq. (12) can be rewritten in the form

$$\frac{d}{dt}(U) + R(U) = 0 \tag{13}$$

where

$$R(U) = J[Q(U) - D(U)] \tag{14}$$

In a four-stage Runge-Kutta scheme, the advance of each variable U from the time level n to $n + 1$ takes the following form:

$$U^{(0)} = U^{(n)}$$
$$U^{(1)} = U^{(0)} - \alpha_1\Delta t R[U^{(0)}]$$
$$U^{(2)} = U^{(0)} - \alpha_2\Delta t R[U^{(1)}] \tag{15}$$
$$U^{(3)} = U^{(0)} - \alpha_3\Delta t R[U^{(2)}]$$
$$U^{(n+1)} = U^{(0)} - \Delta t R[U^{(3)}]$$

with $\alpha_1 = \frac{1}{4}$, $\alpha_2 = \frac{1}{3}$, $\alpha_3 = \frac{1}{2}$.

For computational efficiency the dissipation part was evaluated only once and frozen for the remaining stages. This Runge-Kutta method has an attractive feature in the three-dimensional calculations by requiring only two levels of solution arrays in memory. This scheme is fourth-order accurate in time for linear problems, and is second-order accurate in time for nonlinear problems.[13]

To accelerate the convergence of the time-stepping scheme, devices such as enthalpy damping, local time stepping, and residual smoothing were employed.[11–13] Enthalpy damping is a technique to accelerate the convergence to steady state by modifying the conserved variables at each iteration to force the solution toward the prescribed value. With local time stepping the maximum allowable time step was used at each cell to advance the solution. Finally, residual smoothing was used to reduce the CFL restriction of the solver, thereby allowing the time step to be increased.

Boundary Conditions

On the symmetry plane, numerical boundary conditions stipulated vanishing gradients and zero velocity components normal to the plane since the plane of symmetry must coincide with a stream surface.

At solid walls, the tangential components of the velocity and density were linearly extrapolated from the interior. The pressures along the body surface were obtained from normal momentum equations[14]

$$p_n(\zeta_x^2 + \zeta_y^2 + \zeta_z^2)^{1/2} = (\xi_x\zeta_x + \xi_y\zeta_y + \xi_z\zeta_z)p_\xi + (\eta_x\zeta_x + \eta_y\zeta_y + \eta_z\zeta_z)p_\eta + (\zeta_x^2 + \zeta_y^2 + \zeta_z^2)p_\zeta = -\rho\tilde{u}(\zeta_x u_\xi + \zeta_y v_\xi + \zeta_z w_\xi) - \rho\tilde{w}(\zeta_x u_\zeta + \zeta_y v_\zeta + \zeta_z w_\zeta) \tag{16}$$

where n is the normal direction to the body surface.

The far-field boundary (upstream, lateral, and downstream) condition was treated based on the introduction of Riemann invariants for a one-dimensional flow normal to the boundary.[11,12] If the flow is subsonic in the far field, a fixed and extrapolated Riemann invariants can be expressed as

$$R_\infty = V_{n\infty} - [2a_\infty/(\gamma - 1)] \tag{17}$$

$$R_e = V_{ne} + [2a_e/(\gamma - 1)] \tag{18}$$

where ∞ denotes freestream value, e denotes the values extrapolated from the interior cells to the boundary, V_n is the velocity component normal to the boundary, and a is the speed of sound corresponding to the incoming and outgoing waves.

These Riemann invariants were added and subtracted to provide the actual normal velocity component and speed of sound at the far-field boundary. For the tangential velocity component and entropy, they were either specified as having freestream values or extrapolated from the interior, depend-

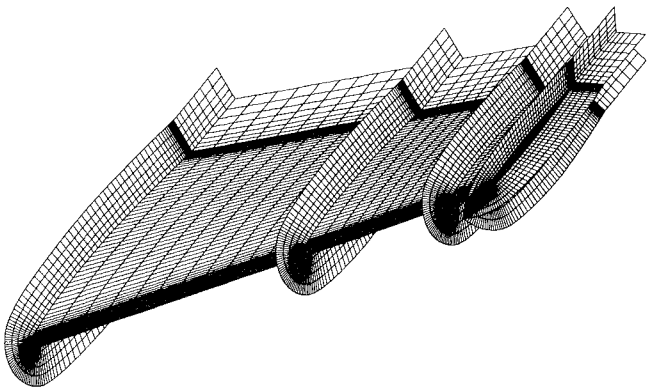

Fig. 2 Partial view of computational grid for ONERA M6 wing (209 × 33 × 49).

ing on whether the flow is of inflow or outflow type at the boundary. With these four flow quantities all the flow variables can be determined at the far-field boundary.

To simulate the passive transpiration effects of a porous wing surface with a cavity located underneath, the normal wall velocity over the porous surface was evaluated using the linear form of the Darcy pressure-velocity law[15]

$$v_w = (\sigma/\rho_\infty u_\infty)(p_c - p_w) \tag{19}$$

where v_w is the normal transpiration velocity at the porous surface, p_c, and p_w are the vent chamber and wall pressures, respectively, and σ is the parameter for geometric porosity. This relationship has been successfully used to simulate the passive control effect in a shock wave/boundary-layer interaction.[3,5-8,15]

Since the net mass flux through the porous surface of area S must be zero for passive flow through the cavity

$$\int_S \rho_w v_w \, dA = 0 \tag{20}$$

As is usually done in the two-dimensional porous airfoil simulations,[5-8] the vent chamber pressure p_c was assumed to be constant. The vent chamber pressure was then computed as

$$p_c = \frac{\int_S \sigma \rho_w p_w \, dA}{\int_S \sigma \rho_w \, dA} \tag{21}$$

Computational Grids

The results for the solid and porous ONERA M6 wing were computed on a C-O type mesh. The grid structure was generated in two phases. First, a C-type two-dimensional grid along a chordwise section was generated using an in-house developed algebraic grid generation procedure. The grids were then distributed along the wingspan using spanwise exponential clustering functions to generate a three-dimensional C-O type mesh. The grids are generated so as to cluster grid points in the leading edge, trailing edge, and rounded-off wingtip regions to provide adequate mesh refinements in those regions of large gradients. The grid so generated had 209 × 33 × 49 grid points. A partial view of the typical mesh, where one can see grid distributions on the wing surface and several selected spanwise sections, is shown in Fig. 2. The far-field boundaries were placed approximately 10 root chords away from the wing.

Results and Discussion

The main objective of this study was to examine the effects of passive control on transonic wing flowfields. Although several inviscid and viscous flow solvers have been developed to compute the two-dimensional airfoil flowfield with passive control,[5-8] to the best of our knowledge none have attempted to simulate the three-dimensional effects of passive control on a transonic wing. This article presents the numerical solutions of transonic flow past porous wing to study the passive control effects. The ONERA M6 wing ($M_\infty = 0.84$, $\alpha = 3.06$ deg) was selected as the basic test configuration, since this model has sufficient experimental data base[16] in case its surface is solid. Since no experimental data was available to compare the computed results of the porous wing, numerical solutions of solid ONERA M6 wing were first obtained to validate the current computational code by comparison with experimental results. The solutions of porous ONERA M6 wing were then obtained and compared with the solid wing solutions.

The following steady flow solutions were obtained by solving the Euler equations on the CRAY-2S supercomputer until the flow properties and the integrated air loads were converged.

Solid ONERA M6 Wing

On this flow it is well known that triple shock wave (weak shock wave, strong shock wave, and their union) exists on the surface and is one of the most standard test cases investigated in the numerous articles.[17-19] The computations for ONERA M6 wing were performed on a mesh that had 209 mesh points in the streamwise direction, 33 mesh points normal to the wing surface, and 49 mesh points in the spanwise direction. A relatively large number of grid points are employed in the spanwise direction since the existence of the triple shock wave on the surface of ONERA M6 wing implies strong gradients are present in this direction.

The computed c_p distributions of this test case are shown in Fig. 3 at six selected spanwise locations along with experimental data. As to the leading-edge expansion, the numerical solutions behaved almost the same as in the experiment at all spanwise locations. However, the weak shock waves (see 65 and 80% semispan locations) were somewhat smeared. This is primarily due to the relatively coarse grid spacing in the midchord region. Computations with more grid points or solution adaptive grid would provide clearer shocks. For the strong shock waves, the Euler solver captured its tendency very well, except that the shock locations were slightly downstream of the experimental data (particularly at 20% semispan location). The inclusion of turbulent boundary-layer effects has to be considered if a more accurate prediction is necessary.

Overall, the predictions of the computations were in favorable agreement with the experiment, and demonstrated the capability of the current Euler solver. The results of computations for the solid ONERA M6 wing also provided a reference case for the porous wing computations.

Porous ONERA M6 Wing

For the passive control on a transonic wing to be effective, the extent of the porous region and the geometric porosity factor σ distribution has to be determined carefully. Since the passive control is generally more effective on the region with larger pressure jump (strong shock), we chose to control the strong shock wave out of the triple shock wave that appears on the upper surface of the solid ONERA M6 wing. In this study the extent of the porous region was determined with reference to the locations of the strong shock wave obtained from the previous solid ONERA M6 wing solutions. For the porous ONERA M6 wing configuration, a portion of the upper surface of the wing ranging from 0.2 chords ahead of the shock to 0.2 chords behind the shock was made porous in the streamwise direction (Fig. 4). In the spanwise direction porosity was distributed from the location of 10% semispan to the location of 92% semispan on the wing upper surface. Since previous studies[6-8] and our numerical experiments indicated

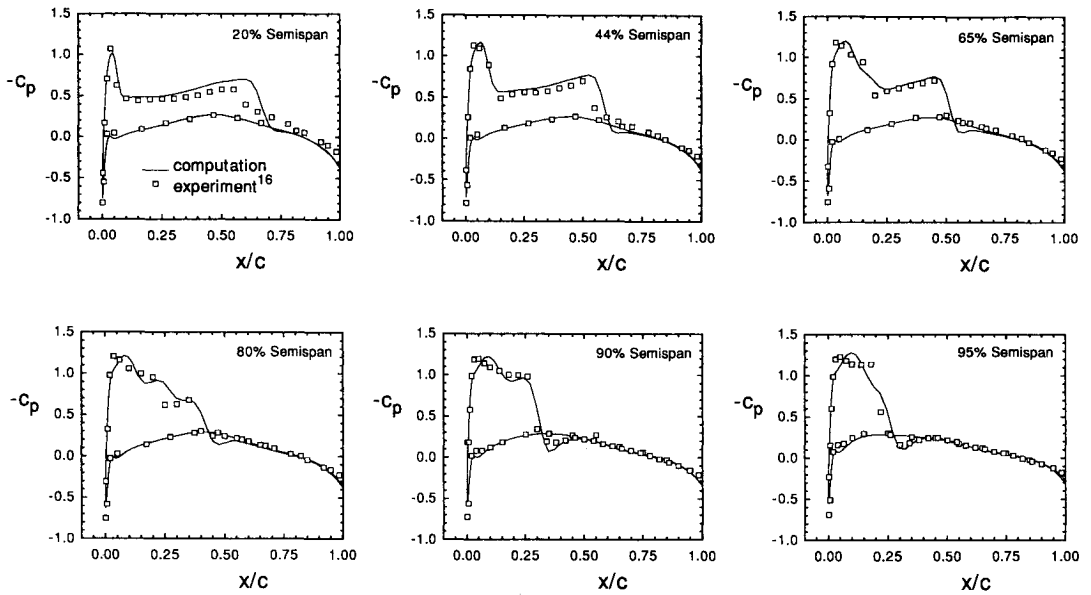

Fig. 3 Comparison of surface pressure distributions between computation and experiment; $M_\infty = 0.84$, $\alpha = 3.06$.

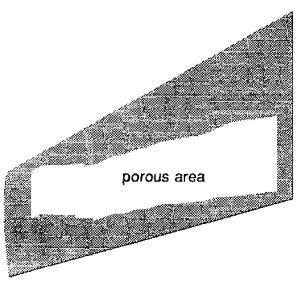

Fig. 4 Porous area on the upper surface of ONERA M6 wing.

that a gradual variation of porosity factor with peak porosity factor under the shock wave is more effective than a uniform porosity factor, the following porosity factor distribution function was employed in the streamwise direction[7,8]:

$$\sigma = \sigma_{\max}\sqrt{\cos\frac{x - x_s}{x_k - x_s}\frac{\pi}{2}}$$

where x_s parameter is the streamwise position of the shock we want to control, and x_k represents either x_1 or x_2, depending on whether x is less or greater than x_s. In this study the peak porosity factor $\sigma_{\max}$ was taken as 0.6, which corresponds to 11% porosity.

The numerical results of the porous ONERA M6 wing, compared with the previously obtained solid wing solutions, are presented in Figs. 5–7. Figure 5 shows the pressure contours for the plane of 60% semispan location and upper surface of the wing. These pressure contours indicate that the nearly normal strong shock wave on the upper surface of the wing is clearly weakened with the presence of porous surface. This substantial reduction in shock strength would suggest a significant reduction in the wave drag component of total drag. Figure 6 shows the normal wall velocity distributions on the porous region, which is a measure of the communications across the shock and through the porous surface. This figure demonstrates that the local mass flux is injected in front of the shock and withdrawn behind the shock. It is also noticed that there exists a spanwise variation of the normal wall velocities, due to the pressure difference along the span; at the inboard stations flow suction is dominant and flow injection becomes stronger towards the outboard stations of the porous wing. The computed normal wall velocities were very small,

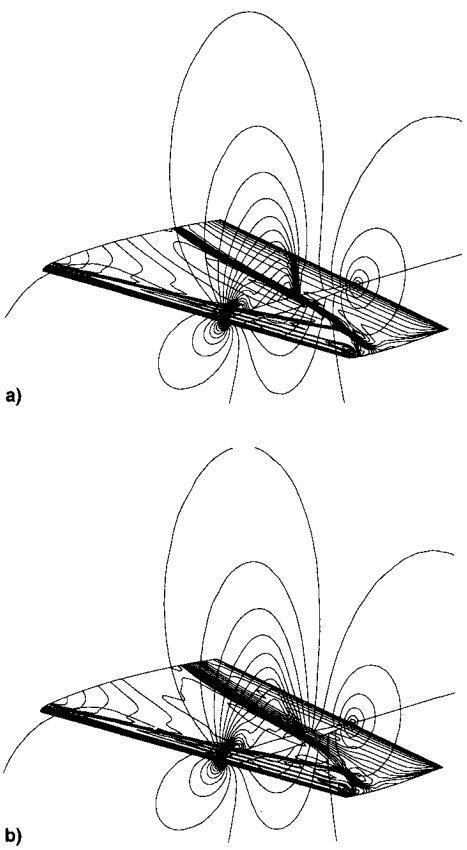

Fig. 5 Pressure contours on upper wing surface: a) solid and b) porous wing.

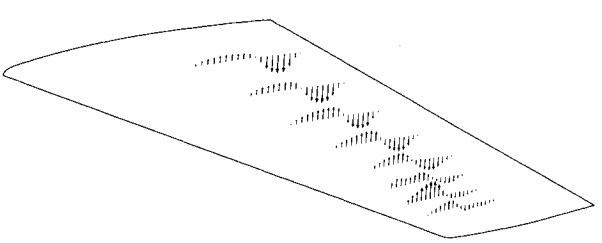

Fig. 6 Normal wall velocity distributions on a porous surface.

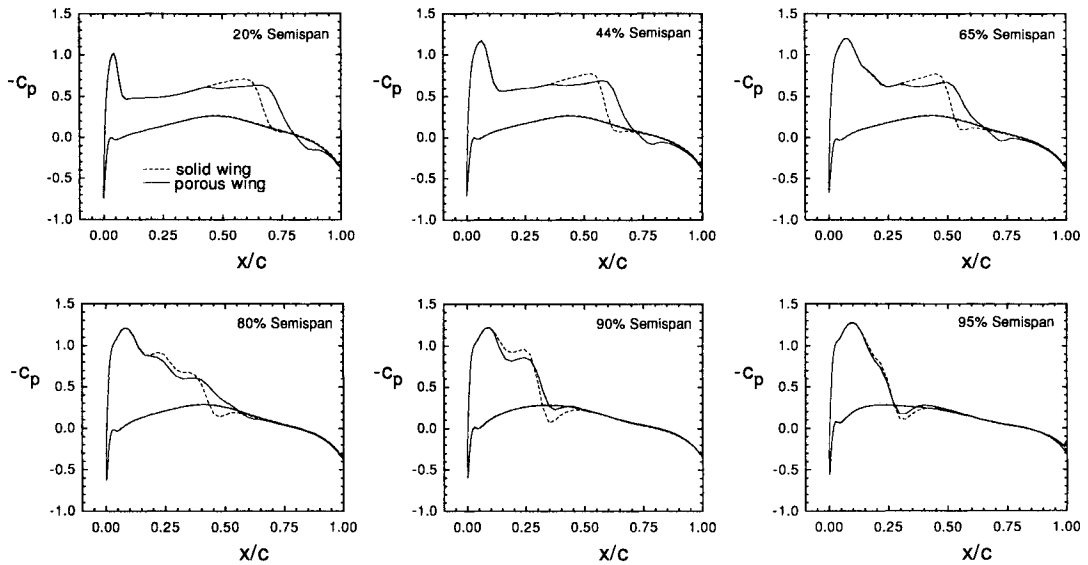

Fig. 7 Comparison of surface pressure distributions between solid wing and porous wing.

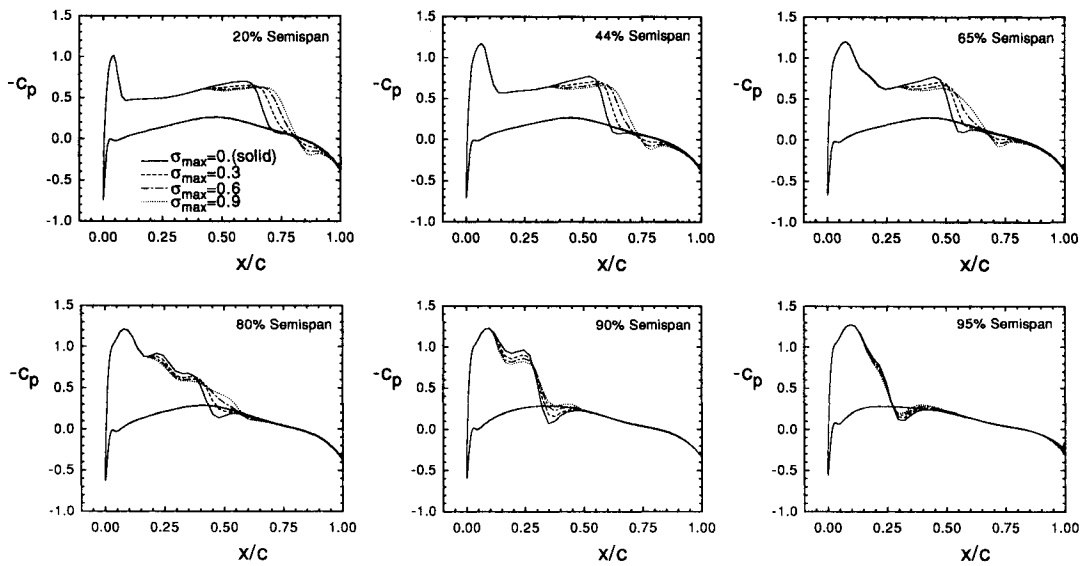

Fig. 8 Effects of varying porosity strength.

less than 3% of the freestream velocity. The computed surface pressure distributions of the porous wing at the six selected spanwise locations are compared with those of the solid wing (Fig. 7). The results also indicate that the passive control over the porous surface weakens the shock and smoothes the pressure gradients. In the previous two-dimensional numerical experiment,[8] which investigated the effects of blowing and suction separately, it was shown that suction behind the shock generally increases the shock strength and moves the shock downstream, whereas injection ahead of the shock weakens the shock. Figure 7 is an example of this phenomena in three dimensions. At the inboard stations (see 20 and 44% semispan locations) the shock has been moved downstream because suction is dominant in this region. However, the strength of the shock has not been increased since a small amount of flow injection exists ahead of the shock. At the outboard stations (see 80 and 90% semispan locations), the surface pressure gradients are significantly reduced due to the dominant flow injection at these locations. The surface pressure distributions at the 95% semispan location are nearly identical with those of the solid wing, since the surface is solid at this location (porosity is distributed up to 92% semispan location.

Finally, the effects of varying the porosity strength on the surface pressure distributions of porous wing are shown in Fig. 8. The results suggest that more substantial reduction in shock strength can be achieved by increasing the porosity strength (with larger σ_{max}). This is because an increase of porosity strength would also increase the recirculating mass flux through the porous surface to provide an augmented control effect.

Conclusions

A computational investigation of the three-dimensional flows about the solid and porous wing was conducted to examine the effects of passive control on the flowfield. For this purpose a three-dimensional Euler code capable of simulating the passive transpiration effects of a porous surface was developed based on a finite volume, multistage time-stepping scheme. The general features of the passive control, such as suppressing the shock strength and relaxation of flow gradients, were found to be consistent with those proved in the previous two-dimensional investigations. In this study the influence of the spanwise variation of mass transpiration on the porous surface was investigated to show that the shock suppression effects are greater at the outboard regions of the porous wing.

This study suggests that the Euler solvers may be used to study passive control techniques on a porous wing. However, they must be verified with more complete flow solutions in-

cluding turbulent boundary-layer effects. Furthermore, detailed experimental data, of on and off surface data as well as aerodynamic force estimations, are required to confirm the passive control concept and to validate numerical solutions.

Acknowledgment

This research was supported by a Grant from Cray Research Inc. to the Systems Engineering Research Institute of Korea.

References

[1]Bahi, L., Ross, J. M., and Nagamatsu, H. T., "Passive Shock Wave/Boundary Layer Control for Transonic Airfoil Drag Reduction," AIAA Paper 83-0137, Jan. 1983.

[2]Nagamatsu, H. T., Dyer, R., and Ficarra, R. V., "Supercritical Airfoil Drag Reduction by Passive Shock Wave/Boundary Layer Control in the Mach Number Range 0.75 to 0.90," AIAA Paper 85-0207, Jan. 1985.

[3]Chokani, N., and Squire, L. C., "Passive Control of Shock/Boundary Layer Interactions: Numerical and Experimental Studies," *Proceedings of the Symposium Transsonicum III*, International Union of Theoretical and Applied Mechanics, Göttingen, Germany, 1989, pp. 24–27.

[4]Krogmann, P., Stanewsky, E., and Thiede, P., "Effects of Suction on Shock/Boundary Layer Interaction and Shock Induced Separation," *Journal of Aircraft*, Vol. 22, No. 1, 1985, pp. 37–42.

[5]Savu, G., Trifu, O., and Dumitrescu, L. Z., "Suppression of Shocks on Transonic Airfoils," *Proceedings of the 14th International Symposium of Shock Tubes and Shock Waves*, Sydney, Australia, 1983, pp. 92–101.

[6]Olling, C. R., and Dulikravich, G. S., "Porous Airfoil Analysis Using Viscous-Inviscid Coupling at Transonic Speeds," *International Journal for Numerical Methods in Fluids*, Vol. 7, Feb. 1987, pp. 103–129.

[7]Chen, C. L., Chow, C. Y., Holst, T. L., and Van Dalsem, W. R., "Numerical Study of Porous Airfoils in Transonic Flow," NASA TM 86713, May 1985.

[8]Chen, C. L., Chow, C. Y., and Van Dalsem, W. R., "Computation of Viscous Transonic Flow over Porous Airfoils," *Journal of Aircraft*, Vol. 26, No. 12, 1989, pp. 1067–1075.

[9]Ma, X., Chang, M. C., Xiao, L. K., and Jiang, J. C., "Computation of Passively Controlled NACA0012 and CAST10 Airfoil Using Navier-Stokes Equation," *The Fifth Asian Congress of Fluid Mechanics*, Taejon, Republic of Korea, 1992, pp. 570–573.

[10]Hartwich, P. M., "Euler Study on Porous Transonic Airfoils with a View Toward Multipoint Design," AIAA Paper 91-3286, Sept. 1991.

[11]Jameson, A., Schmidt, W., and Turkel, E., "Numerical Solutions of the Euler Equations by Finite Volume Methods Using Runge-Kutta Time-Stepping Schemes," AIAA Paper 81-1259, June 1981.

[12]Jameson, A., and Baker, T. J., "Solutions of the Euler Equations for Complex Configurations," AIAA Paper 83-1929, July 1983.

[13]Swanson, R. C., and Turkel, E., "A Multistage Time-Stepping Scheme for the Navier-Stokes Equations," AIAA Paper 85-35, Jan. 1985.

[14]Pulliam, T. H., and Steger, J. L., "Implicit Finite-Difference Simulations of Three-Dimensional Flow," *AIAA Journal*, Vol. 18, No. 2, 1980, pp. 159–167.

[15]Kim, I., and Chokani, N., "Navier-Stokes Study of a Supersonic Cavity Flowfield with Passive Control," *Journal of Aircraft*, Vol. 29, No. 2, 1990, pp. 217–223.

[16]Schmitt, V., and Charpin, F., "Pressure Distributions on the ONERA-M6 Wing at Transonic Mach Numbers," AGARD-AR-138, May 1979, Chap. B-1.

[17]Takakura, Y., Ishiguro, T., and Ogawa, S., "On the Recent Difference Schemes for the Three-Dimensional Euler Equations," AIAA Paper 87-1151, June 1987.

[18]Vatsa, V. N., "Accurate Numerical Solutions for the Transonic Viscous Flow over Finite Wings," *Journal of Aircraft*, Vol. 24, No. 6, 1987, pp. 377–385.

[19]Deese, J. E., and Agarwal, R. K., "Navier-Stokes Calculations of Transonic Viscous Flow About Wing/Body Configurations," *Journal of Aircraft*, Vol. 25, No. 12, 1988, pp. 1106–1112.